Journal of Ovarian Research

RESEARCH

Open Access

Single-cell RNA sequencing reveals the role of GTF2F2 in ovarian cancer oncogenesis and progression

Haiyang Du[1,2], Gao Si[3], Jiqing Si[4], Xuejie Song[1,2] and Fuchun Si[1,2*]

Abstract

Background Ovarian cancer is one of the most common malignancies of the female reproductive system and is associated with poor prognosis. This study aimed to utilize single-cell RNA sequencing to investigate the heterogeneity of malignant epithelial cells in ovarian cancer, focusing on their potential functions and the implications for treatment and prognosis.

Methods Single-cell RNA sequencing data were clustered using a single-cell transcriptome clustering method, and malignant epithelial cells were identified through copy number variation analysis. The interaction patterns between different malignant subpopulations and immune/stromal cells were analyzed using cell-to-cell communication analysis. A risk score (URS) model based on the UBE2C + epithelial subpopulation was then constructed through LASSO and multivariable Cox regression. High and low URS groups were compared in terms of tumor mutational burden (TMB), survival outcomes, and drug sensitivity. Finally, the role of GTF2F2 in ovarian cancer progression was validated through gene knockdown experiments in an ovarian cancer cell line (ES-2).

Results Three major malignant epithelial cell subpopulations were identified (TMSB4X + Epi, TSC22D1 + Epi, and UBE2C + Epi). The UBE2C + Epi subpopulation exhibited higher stemness and greater invasive potential. The constructed URS model effectively stratified patients into high- and low-risk groups, with the high-risk group displaying a higher TMB level ($p = 0.00011$). Drug sensitivity predictions indicated that osimertinib, rapamycin, and dihydrorotenone might have stronger inhibitory effects in the high-risk group, whereas ERK inhibitors were more effective in the low-risk group. Functional assays demonstrated that GTF2F2 knockdown significantly suppressed ovarian cancer cell migration and invasion. Western blot analyses further showed elevated E-cadherin and reduced N-cadherin expression, suggesting that GTF2F2 may promote epithelial-mesenchymal transition (EMT).

Conclusion The risk score model established in this study offers a novel framework for patient stratification and personalized therapy. Notably, the identification of the UBE2C + Epi subpopulation and key genes such as GTF2F2 highlights potential diagnostic and therapeutic targets, shedding light on the pathogenesis of ovarian cancer and paving the way for precision medicine approaches.

Keywords Single-cell RNA sequencing, Ovarian cancer, UBE2 C + Epi, GTF2 F2, EMT

*Correspondence:
Fuchun Si
sifc2000@hotmail.com
Full list of author information is available at the end of the article

Ovarian cancer (OV) is among the most lethal gynecologic malignancies, typically diagnosed at an advanced stage, which results in suboptimal therapeutic outcomes [1]. Clinically, approximately one-third of OV patients present with ascites, further complicating disease management and treatment [2]. Owing to its marked heterogeneity, OV exhibits significant variations in histological subtypes, molecular characteristics, and the tumor microenvironment (TME), all of which substantially influence therapeutic responses and clinical outcomes [3]. Currently, the standard treatment paradigm for OV involves surgical intervention in combination with platinum-based chemotherapy; in patients with advanced disease and ascites, this comprehensive approach can extend median survival to 16–22 months [4]. However, a subset of patients develop platinum resistance immediately following initial therapy, and nearly all recurrent cases eventually progress to platinum-resistant OV [5]. The emergence of chemoresistance, coupled with the lack of reliable early diagnostic strategies, contributes to the poor overall prognosis and persistently high recurrence rates observed in OV. Therefore, in-depth investigation of the molecular mechanisms and optimization of therapeutic strategies remain urgently needed.

In recent years, single-cell sequencing (scRNA-seq) technologies have rapidly gained traction in cancer biology research, offering novel insights into various malignancies (melanoma, glioblastoma and colorectal cancer) [6–8]. Through scRNA-seq, investigators can dissect tumor heterogeneity, the immune TME, and underlying mechanisms of drug resistance at the single-cell level [9]. However, the systematic application of scRNA-seq to clinical OV samples remains limited, underscoring the need for further research to elucidate its complex pathobiological features.

In this study, we collected omental tissue samples from six patients with OV with scRNA-seq data. We focused on malignant epithelial cells characterized by high copy number variation (CNV), aiming to unravel their intratumoral molecular diversity and developmental trajectories. By integrating functional enrichment and transcription factor (TF) analyses, we sought to uncover the potential regulatory networks governing these cells. Simultaneously, we incorporated data from The Cancer Genome Atlas (TCGA) to construct a prognostic risk model, thereby evaluating immune TME differences in OV and their impact on clinical outcomes. Our key objectives were to (1) systematically delineate the intratumoral heterogeneity of malignant epithelial cells in peritoneal metastases of OV, (2) identify potential biomarkers and clarify their associations with prognosis, and (3) uncover the molecular mechanisms of interactions between distinct cell subpopulations and the TME, ultimately providing new avenues for precision therapy.

Methods

OV data acquisition

The single-cell RNA sequencing (scRNA-seq) data used in this study were obtained from the GEO database (NCBI Gene Expression Omnibus, https://www.ncbi.nlm.nih.gov/geo/query/acc.cgi?acc=GSE173682) under accession number GSE173682, which includes omental tissue samples from six patients with ovarian cancer (OV). Bulk RNA-seq expression profiles and clinical data were retrieved from The Cancer Genome Atlas (TCGA) OV cohort (https://portal.gdc.cancer.gov/), comprising a total of 427 valid samples, to construct the prognostic model.

Data quality control and dimensionality reduction

Raw count matrices were processed using the Scanpy package (v.1.9.1, Python 3.8) [10]. Suspected doublets were identified and filtered out using Scrublet (v.3.0) with default parameters [9]. Low quality cells were further removed based on the following criteria, (1) 300–8000 genes detected per cell, (2) 500–50,000 total UMI counts per cell, (3) Mitochondrial gene expression < 20%. After preliminary filtering, total expression for each cell was normalized using *sc.pp.normalize_total*, followed by log transformation (*sc.pp.log1p*) for additional standardization. We then selected highly variable genes using the *highly_variable_genes* function and flavour = seurat_v3. Harmony (v.0.0.10) was applied (with the parameter theta = 2) to correct for batch effects across different individuals [11]. Clustering was performed with the Leiden algorithm (resolution = 0.1), and visualization was achieved via UMAP (n_neighbors = 15, min_dist = 0.5).

Malignant epithelial cell identification using inferCNV

To distinguish non-malignant and malignant epithelial cells in the OV, we employed "InferCNVpy" (Https://github.com/broadinstitute/inferCNV) to infer CNVs across different cell types. Immune cells served as the reference group in inferCNV, and elevated CNV levels were indicative of malignant epithelial cells. Malignant epithelial cells thus identified were re-clustered using the Leiden algorithm.

Heterogeneity of OV subpopulation

The function *sc.tl.rank_genes_groups* was used to identify differentially expressed genes in each subpopulation. GO Biological Process enrichment analysis was subsequently performed using the GSEApy Python package. Additionally, gene set enrichment analysis (GSEA) was conducted

using the KEGG_2021_Human dataset to rank gene function across subpopulation.

Subcluster stemness analysis and trajectory analysis

To evaluate differences in differentiation status across OV subpopulation, we utilized CytoTRACE 2 (v.1.1.0) to compute CytoTRACE scores for each subpopulation, thereby inferring their respective differentiation level [12]. We then employed the pySCENIC algorithm to explore transcription factors (TFs) and regulators within each subcluster [13]. GRNBoost was first applied to establish putative TF–target gene relationships, followed by DNA motif analysis to identify potential direct binding targets. AUCell was used to evaluate the activity of each regulator in individual cells, and the top five TFs with the highest scores were selected.

Cell–cell communication analysis

To investigate the complex intercellular communication among subpopulation, we employed the CellPhoneDB software package (v.1.6.1) to assess cell–cell interactions, focusing primarily on signaling pathways and receptor–ligand interactions [14].

Construction and validation of a novel prognostic risk model

The top 500 genes of UBE2C + Epi were screened related to the OS of TCGA patients using a univariate Cox analysis ($P < 0.05$). The least absolute shrinkage and selection operator (LASSO) regression can identify the most important elements to improve the prediction accuracy of statistical model. Therefore, after identifying the prognosis related genes. The risk score for each sample was calculated through linearly multiplying the expression level with Coef of each gene, according to the following formula: Risk score = (Coef. of gene 1 × expression of gene 1) + (Coef. of gene 2 × expression of gene 2) + … + (Coef. of gene × expression of gene n). Patients were then divided into high and low risk score groups based on the median Risk Score. Kaplan–Meier (KM) survival curves and receiver operating characteristic (ROC) curves were generated to validate the model's prognostic value.

Immune infiltration analysis and functional enrichment analysis

We applied the CIBERSORT algorithm to investigate immune infiltration in both the high.

and low risk groups, thereby elucidating the relationship between immune-infiltrating cells and prognostic genes [15]. In addition, we evaluated the TIDE (Tumor Immune Dysfunction and Exclusion) scores for both groups and compared immune checkpoint–related gene expression between the high and low risk groups using the Wilcoxon test.

To further explore heterogeneity between the high and low risk groups, we identified differentially expressed genes using the DESeq2 package (v.1.46.0). Next, we utilized the clusterProfiler R package (v.4.6.2) to perform Kyoto Encyclopedia of Genes and Genomes (KEGG) pathway analysis and to conduct functional enrichment for GO Biological Process [16].

Gene mutation analysis

Somatic mutation data for OV were obtained from the TCGA database. We used the maftools package (v.2.22.0) [15] to calculate tumor mutational burden (TMB) scores across different samples and performed Spearman's correlation analysis to examine the relationship between TMB and the risk score. Based on the median TMB value, samples were categorized into high and low TMB groups, followed by Kaplan–Meier survival analysis to explore prognostic differences [17].

Drug sensitivity assessment

We employed the pRRophetic R package (v.0.5) to evaluate the half-maximal inhibitory concentration (IC_{50}) of various chemotherapeutic agents in different groups [18].

Cell lines and culture

ES-2 cells were obtained from the Cell Bank of the Committee on Type Culture Collection of the Chinese Academy of Sciences. Cells were cultured in RPMI 1640 medium (Gibco, USA) supplemented with 10% fetal bovine serum and 1% penicillin/streptomycin. The incubation conditions were 37 °C with 5% CO2 and 95% relative humidity.

Construction and transfection of shRNA

To achieve effective knockdown of GTF2F2 gene expression, we first designed shRNA constructs based on the sequences of siRNA1 (5′-CGAGCTGATAAACAACAT GTT-3′) and siRNA2 (5′-GCTCCTAGAGAACACCCA TTT-3′). These oligonucleotides were cloned into the pLKO.1-TRC vector and verified by Sanger sequencing. To serve as a negative control, we also included a scramble shRNA (Plasmid #1864) that has no target sequence in the human genome. The recombinant plasmid, together with psPAX2 and pMD2.G packaging plasmids, was co-transfected into 293 T cells using Lipofectamine 3000 (Invitrogen, USA) per the manufacturer's instructions to generate lentiviruses. Seventy-two hours post-transfection, the lentivirus-containing supernatant was collected and filtered through 0.45 μm filters.

Viral supernatant was then added to ES-2 cells at logarithmic growth phase, along with 4 μg/mL Polybrene to

enhance transduction efficiency. Forty-eight hours later, the medium was replaced, and 8 μg/mL puromycin was added for stable clone selection. Approximately 7 days post-infection, non-transduced cells had died, while infected cells continued to proliferate. Knockdown efficiency was assessed in the resulting stable cell lines by extracting total RNA and measuring GTF2F2 mRNA levels via RT-qPCR, using RT-qPCR primer sets (GTF2F2_qpcr_F: 5′-AACTGCGGATTGCCAAGACTCA-3′, GTF2F2_qpcr_R: 5′-GGAGCACTGACTGAAGCTGGTT-3′). The stable ES-2 cell line with GTF2F2 knockdown was then used for further experiments.

Wound healing assay

Transfected cells were seeded and cultured in 6-well plates. Upon reaching ~ 95% confluence, a sterile 200 μL pipette tip was used to create a straight scratch on the cell monolayer. The wells were gently rinsed with PBS to remove nonadherent cells and debris, then replenished with fresh medium to support cell growth. Images of the scratch were taken at 0 and 48 h from the same perspective to assess wound closure.

Transwell assay

Cell migration and invasion were evaluated using Transwell chambers with 8.0 μm pore membranes (Corning, USA). For the invasion assay, the upper membrane was pre-coated with Matrigel (BD Biosciences, 356,234). Cells (2.0×10^5/mL) were suspended in serum-free medium and placed in the upper chambers, while the lower chambers contained complete medium with 10% fetal bovine serum. After 48 h of incubation, cells on the lower surface of the membranes were fixed in 4% paraformaldehyde, stained with crystal violet, and counted under a microscope.

Western bolt

Total protein was extracted from cells (including the GTF2F2 knockdown and corresponding control groups) using RIPA lysis buffer supplemented with a protease inhibitor cocktail. The protein concentration was quantified via a bicinchoninic acid (BCA) assay (Beyotime, China). Equal amounts of protein (20 μg) were separated by SDS-PAGE (10% gel) and transferred onto polyvinylidene difluoride (PVDF) membranes (Millipore, USA). The membranes were blocked with 5% non-fat milk in TBS-T buffer (20 mM Tris–HCl, 150 mM NaCl, 0.1% Tween 20, pH 7.4) for 2 h at room temperature and then incubated overnight at 4 °C with the following primary antibodies: E-cadherin (3195S, Cell Signaling Technology, 1:1000), N-cadherin (13116S, Cell Signaling Technology, 1:1000), and β-Actin (4970S, Cell Signaling Technology, 1:1000) as a loading control. After three washes in TBS-T, the membranes were incubated with horseradish peroxidase (HRP)-conjugated secondary antibodies (Anti-rabbit IgG, HRP-linked 7074S, Cell Signaling Technology, 1:2000) for 2 h at room temperature. Protein bands were visualized using an enhanced chemiluminescence (ECL) reagent (SQ201, Epizyme Biotech) and imaged on a ChemiDoc imaging system (Bio-Rad, USA). Band intensity was quantified using ImageJ software (NIH, USA), and the relative expression levels of E-cadherin and N-cadherin were normalized to β-Actin. The experiment was performed in triplicate to ensure reproducibility.

Statistical analysis

Statistical analyses were performed using R software (version 4.4.0). Wilcoxon tests and Pearson correlation coefficients were used to evaluate the significance of differences among groups. Significance levels were denoted as $^{*}P<0.05$, $^{**}P<0.01$, $^{***}P<0.001$, $^{****}P<0.0001$. "ns" indicates no significant difference.

Results

Single-cell TME landscapes of OV

After rigorous quality filtering, including the removal of doublets and low quality cells, and batch-effect correction, a total of 31,691 high quality cells were retained for downstream analysis. The overall experimental design in this study is indicated as a diagram (Fig. 1). We applied the Leiden clustering algorithm (resolution = 0.1) and visualized the resulting clusters using UMAP (Fig. 2A). Cluster annotations were confirmed by comparing the average expression level of canonical markers in our dataset to those known in the literature, which revealed major cell compartments including Epithelial cells (cluster 0, marked by EPCAM and KRT19), Fibroblasts (clusters 1 and 4, marked by C11orf96 and IGFBP7), T cells (cluster 2, marked by CXCR4 and CD7), Macrophages (cluster 3, marked by CD68 and FCER1G), Endothelial cells (cluster 5, marked by ANGPT2 and ESAM), and plasma cells (cluster 6, marked by IGHG1, IGHG3, and IGKC) (Fig. 2B,C).

To better understand the TME landscapes of OV, we examined the proportions of each cell type in Carcinoma, Endometrioid, GST, and High grade serous samples (Fig. 1D). Overall, Epithelial cells comprised approximately 30% of the cell population in all subtypes. However, Macrophage proportion in Endometrioid tumors was only 0.60%, which was lower than in the other types. We next compared cell-type distributions across different clinical stages (Fig. 2E). While the fraction of Epithelial cells remained relatively stable, T cells and Macrophages exhibited notable fluctuations in advanced stages, suggesting dynamic changes

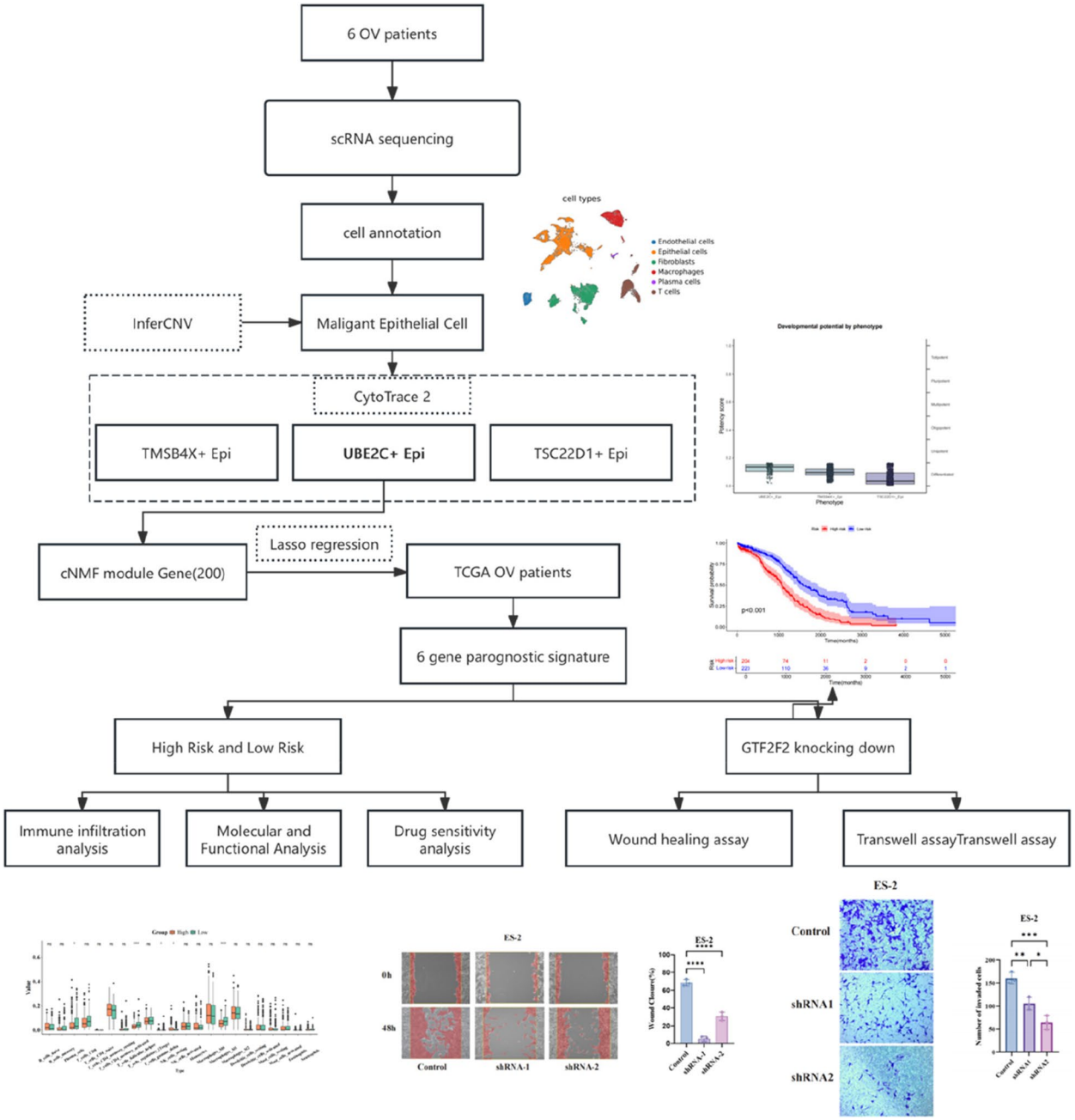

Fig. 1 Flow chart of patient selection and data extraction

in the immune TME during disease progression. To elucidate the functional properties of each cell type in OV, we performed GO-BP enrichment analysis on the differentially expressed genes of each cluster (Fig. 2F). Epithelial cells were enriched in pathways such as Desmosome Organization and Negative Regulation of TGF-β Receptor Signaling Pathway, suggesting their roles in maintaining tissue structural integrity and restraining abnormal proliferative signals. Fibroblasts exhibited significant enrichment in Vascular Associated Smooth Muscle Contraction and Skin Morphogenesis, underscoring their importance in matrix remodeling and angiogenesis. T cells were highly associated with Alpha–Beta T Cell Activation and Protection From Natural Killer Cell Mediated Cytotoxicity, highlighting their involvement in immune surveillance and potential immune evasion mechanisms. Macrophages were enriched in Humoral Immune Response Mediated By

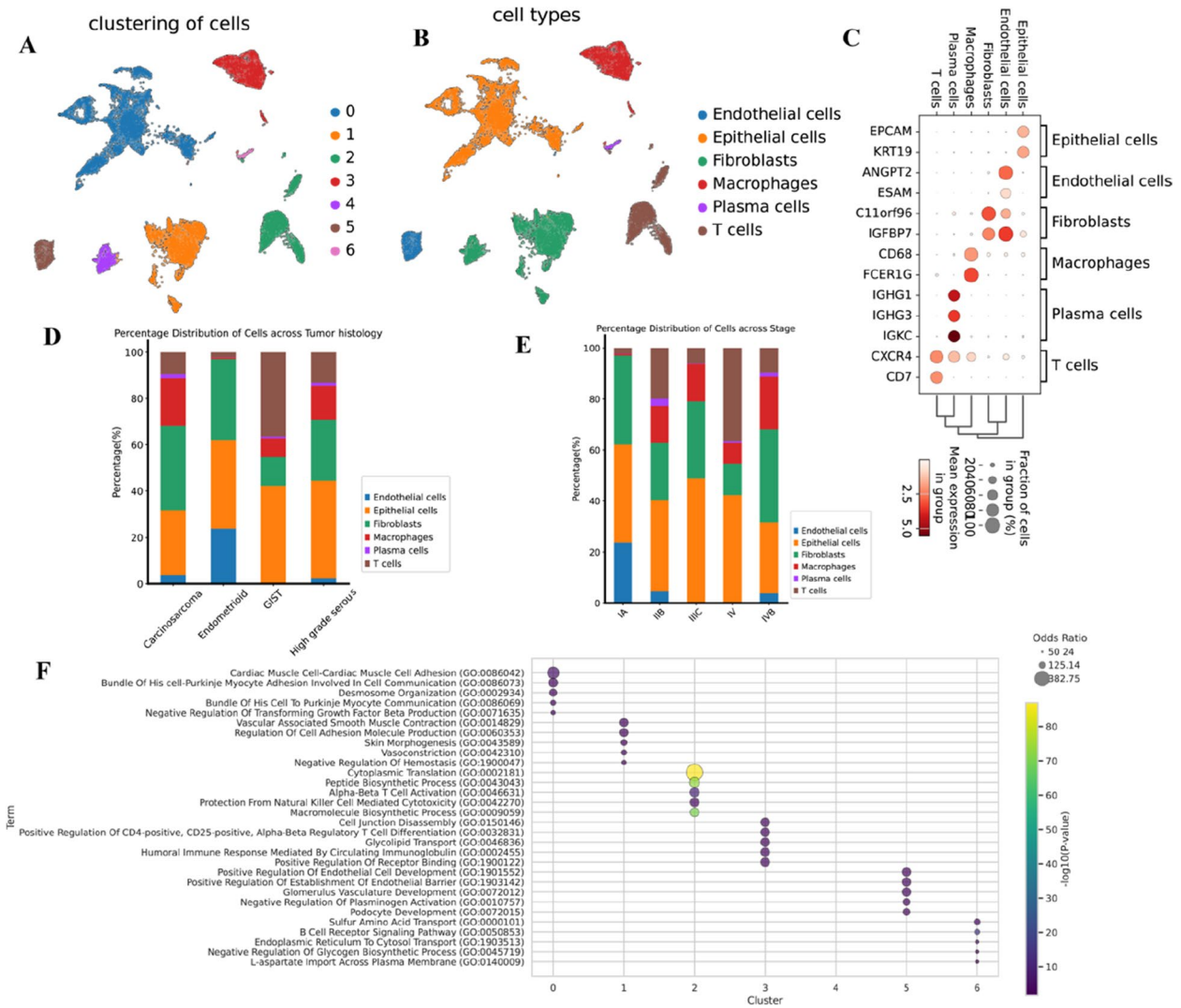

Fig. 2 Major cell types in OV. **A** UMAP visualization of seven distinct clusters encompassing 31,691 high quality cells **B** UMAP plot displaying the distribution of six identified cell types. (**C**) Dot plot showing the expression patterns of marker genes for each cell type. **D** Bar chart comparing the proportions of each cell type among different histological subtypes. **E** Bar chart illustrating the distribution of cell types across various clinical stages. **F** Bubble chart presenting the GO biological process enrichment analysis of differentially expressed genes in each cell type

Circulating Immunoglobulin and Cell Junction Disassembly, reflecting their dual functions in immune regulation and mediating changes in intercellular communication or adhesion. Endothelial cells, known to be closely linked to angiogenesis, showed enrichment in Positive Regulation of Endothelial Cell Development, whereas Plasma cells exhibited enrichment in the B Cell Receptor Signaling Pathway, emphasizing their pivotal role in antibody production. Collectively, these findings validate the accuracy of our cell-type annotations and reveal the cooperative interactions of different cell subsets in shaping the OV TME, thereby offering valuable insights into disease pathogenesis.

Identification of malignant epithelial cells in OV

We utilized InferCNVpy to analyze CNVs across all cells. Cells exhibiting significantly elevated CNV profiles were classified as malignant cells (Figure S1). A total of 4,203 malignant epithelial cells were retained. Dimensional reduction and clustering further segregated these epithelial cells into 3 subpopulations, TMSB4X + Epi (2,239 cells, cluster 0), TSC22D1 + Epi (1,627 cells, cluster 1), and UBE2C + Epi (337 cells, cluster 2) (Fig. 3A). Further analysis of subpopulation distributions across different clinical stages revealed a marked increase in the proportion of UBE2C + Epi cells in advanced disease (Stage IV), reaching up to 77.45%, while TMSB4X + Epi cells also

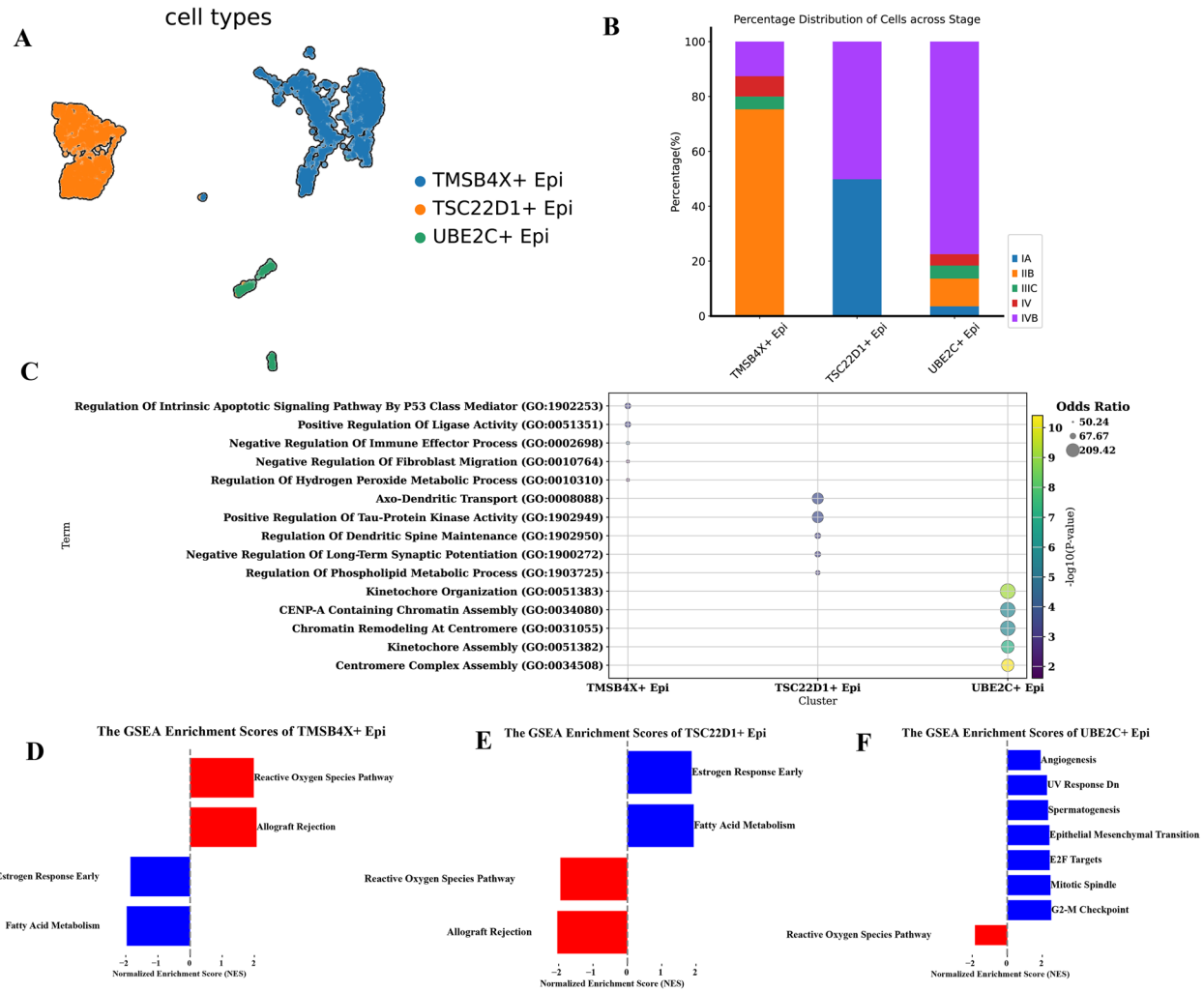

Fig. 3 Identification and functional analysis of malignant epithelial cells in OV. **A** UMAP visualization of 4,203 malignant epithelial cells identified by CNV profiling, divided into 3 subpopulations: TMSB4X + Epi (orange), TSC22D1 + Epi (blue), and UBE2C + Epi (green). **B** Relative proportions of each subpopulation across different clinical stages. **C** Bubble plot showing GO biological process enrichment of differentially expressed genes in the 3 subpopulations. **D**–**F** GSEA results for each subpopulation: red bars indicate positive enrichment, and blue bars indicate negative enrichment

exhibited a modest rise (~4.15%) in advanced stage of OV (Fig. 3B). These observations suggest that both subpopulations may be closely associated with tumor progression and heightened invasiveness, warranting further functional investigation.

To delineate the functional characteristics of the 3 epithelial subpopulations, we performed GO Biological Process enrichment analysis on the top 200 highly expressed genes within each subpopulation (Fig. 3C). TMSB4X + Epi cells were significantly enriched in pathways such as Regulation of Intrinsic Apoptotic Signaling Pathway and Negative Regulation of Immune Effector Process, suggesting a pivotal role in regulating apoptosis and immune evasion. TSC22D1 + Epi cells displayed enrichment in neuronal and dendritic processes, including Axo-Dendritic Transport and Regulation of Dendritic Spine Maintenance," as well as phospholipid metabolic pathways, implying a potential for high cellular plasticity and membrane remodeling. Meanwhile, UBE2C + Epi cells were strongly associated with cell cycle and chromosomal stability pathways, such as Kinetochore Organization and CENP-A Containing Chromatin Assembly. Considering their elevated CNV levels, these cells may drive tumor progression through accelerated cell division.

To gain deeper insights into the molecular distinctions among these subpopulations, we performed GSEA on their overall transcriptomic profiles (Figs. 3D–F). TMSB4X + Epi cells showed significant upregulation

of the Reactive Oxygen Species Pathway and Allograft Rejection, while Fatty Acid Metabolism and Estrogen Response Early were notably downregulated, suggesting a potential advantage in coping with oxidative stress and immune challenges. In contrast, TSC22D1 + Epi cells exhibited elevated Fatty Acid Metabolism and Estrogen Response, along with decreased ROS pathway activity, indicating a metabolic and hormonal dependency but reduced oxidative defense. Notably, UBE2C + Epi cells strongly activated pathways related to Angiogenesis, Mitotic Spindle, E2F Targets, and EMT, while concurrently suppressing the ROS pathway, implying a high proliferative and invasive capacity alongside tolerance to oxidative stress. Collectively, these GSEA findings corroborate the results of the GO analysis and further underscore the distinct functional trajectories of each subpopulation in OV progression.

In summary, the TMSB4X + Epi subpopulation may facilitate tumor cell survival through heightened immune evasion and oxidative stress responses, while the TSC22D1 + Epi subpopulation appears more dependent on lipid metabolism and estrogen signaling. The UBE2C + Epi subpopulation exhibits robust proliferative, invasive, and oxidative stress-resistant phenotypes, becoming dominant in advanced-stage tumors. These distinct functional profiles shed light on the multifaceted pathogenic mechanisms underpinning OV and pave the way for targeted therapeutic interventions, such as inhibiting UBE2C-mediated cell cycle pathways or modulating ROS-associated mechanisms.

Stemness and gene regulatory network analyses of malignant epithelial subpopulations

To further elucidate the stemness properties and developmental trajectories of the 3 malignant epithelial subpopulations, we performed CytoTRACE analysis, which assigns higher scores to cells with stronger stemness features and lower differentiation states. The UBE2C + Epi exhibited the highest CytoTRACE scores overall, suggesting a more *early* or *undifferentiated* phenotype, whereas TMSB4X + Epi and TSC22D1 + Epi displayed relatively lower scores (Figs. 4A–C). These findings were consistent with slingshot pseudotime analysis, indicating that UBE2C + Epi cells may play a pivotal role in driving tumor proliferation and invasion.

Next, we employed pySCENIC to infer gene regulatory networks for each subpopulation by identifying TFs and their co-expressed gene sets. Based on Regulon Specificity Score, we extracted the top 5 TFs for each cluster (Figs. 4D–F). TMSB4X + Epi showed high activity of SPI1, IRF1, ZNF524, IRF8, and TCF7; UBE2C + Epi was characterized by SMARCC2, MSC, NFATC2, ZBTB24, and SOX7, whereas TSC22D1 + Epi was enriched in FOXC1, LEF1, JUN, ATF3, and FOS. Heatmap visualization revealed that ZNF524, LEF1, and MSC were the most active TFs in TMSB4X + Epi, TSC22D1 + Epi, and UBE2C + Epi, respectively (Fig. 4G). Together, our CytoTRACE and pySCENIC analyses suggest that UBE2C + Epi cells may serve as key drivers of early tumor evolution and aggressive behavior in OV, whereas TMSB4X + Epi and TSC22D1 + Epi appear more terminally differentiated with lower stemness scores. Future experimental validation of MSC, LEF1, and other critical TFs could shed further light on the role of these subpopulations in OV progression and provide potential therapeutic targets.

Cell–Cell communication analysis

To elucidate the interaction patterns between the 3 malignant epithelial subpopulations and other key cell types within OV TME, we employed CellPhoneDB to systematically analyze ligand–receptor pairs (Figs. 5A–C). This method identifies significant interactions ($P < 0.05$) and visualizes them according to ligand or receptor expression levels in each cell type. In addition to the 3 epithelial subpopulations, this analysis included endothelial cells, Fibroblasts, Macrophages, plasma cells, and T cells, providing a comprehensive overview of the TME's cellular components.

UBE2C + Epi cells exhibited multiple significant interactions with endothelial cells, including VEGFB-FLT1, VEGFB-NRP1, TGM2-ADGRG1, and the COL18A1–integrin α2β1 complex (Fig. 5A). Most of these interactions are closely associated with angiogenesis and ECM remodeling, implying a potential role for UBE2C + Epi in promoting neovascularization and tumor matrix reorganization. Additionally, the PPIA-BSG and MPZL1-MPZL1 pairs between UBE2C + Epi and fibroblasts suggest possible regulation of collagen networks and stromal homeostasis. Meanwhile, interactions with macrophages—such as APP-CD74, CD99-PILRA, and PLAU-PLAUR—may be involved in immune evasion and the modulation of inflammatory responses. Similar to UBE2C + Epi, TMSB4X + Epi cells also engaged in multiple pro-angiogenic interactions with endothelial cells (VEGFB-NRP1, VEGFB-FLT1, TGM2-ADGRG1) (Fig. 5B). Notably, SEMA3C-NRP2 has been implicated in both angiogenesis and neural remodeling, underscoring TMSB4X + Epi's potential role in tumor vascularization and ECM restructuring. This subpopulation also demonstrated key interactions with macrophages (APOA1-ABCA1, APP-CD74, and CD99-PILRA), possibly affecting lipid transport, antigen presentation, and innate immunity. In addition, PPIA-BSG and PLAU-PLAUR interactions with fibroblasts may facilitate ECM degradation and remodeling, highlighting TMSB4X + Epi's

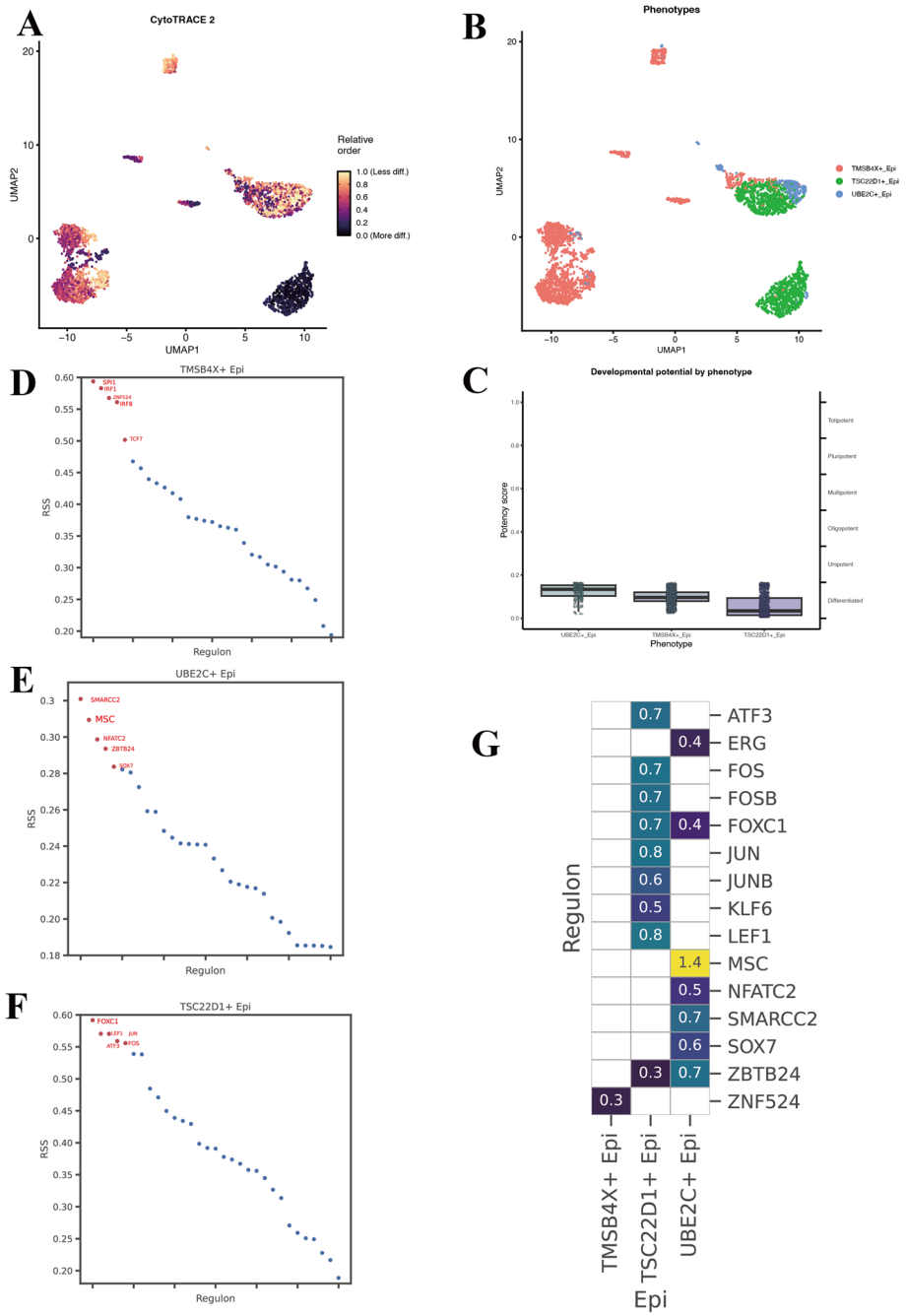

Fig. 4 CytoTRACE and Transcription Factor Network Analyses of Malignant Epithelial Subpopulations. **A** CytoTRACE analysis results, with colors transitioning from dark to light to indicate lower to higher stemness scores. **B** UMAP plot showing the three malignant epithelial subpopulations. **C** CytoTRACE scores for each subpopulation, where higher scores reflect greater stem cell–like potential. **D**–**F** pySCENIC-based gene regulatory network inference; dot plots illustrate the top-ranked transcription factors in each subpopulation according to Regulon Specificity Score. **G** Heatmap comparing the most active TFs across different subpopulations, depicted as Z-scores

capacity to reshape the tumor microenvironment for its own proliferation. TSC22D1 + Epi cells also displayed an extensive repertoire of pro-angiogenic and ECM-related interactions with endothelial cells (VEGFB-NRP1, VEGFB-FLT1, TGM2-ADGRG1, and COL18A1–integrin α2β1 complex), indicating a significant role in tumor vascularization and matrix remodeling (Fig. 5C). Interactions with macrophages (APP-CD74, CD99-PILRA,

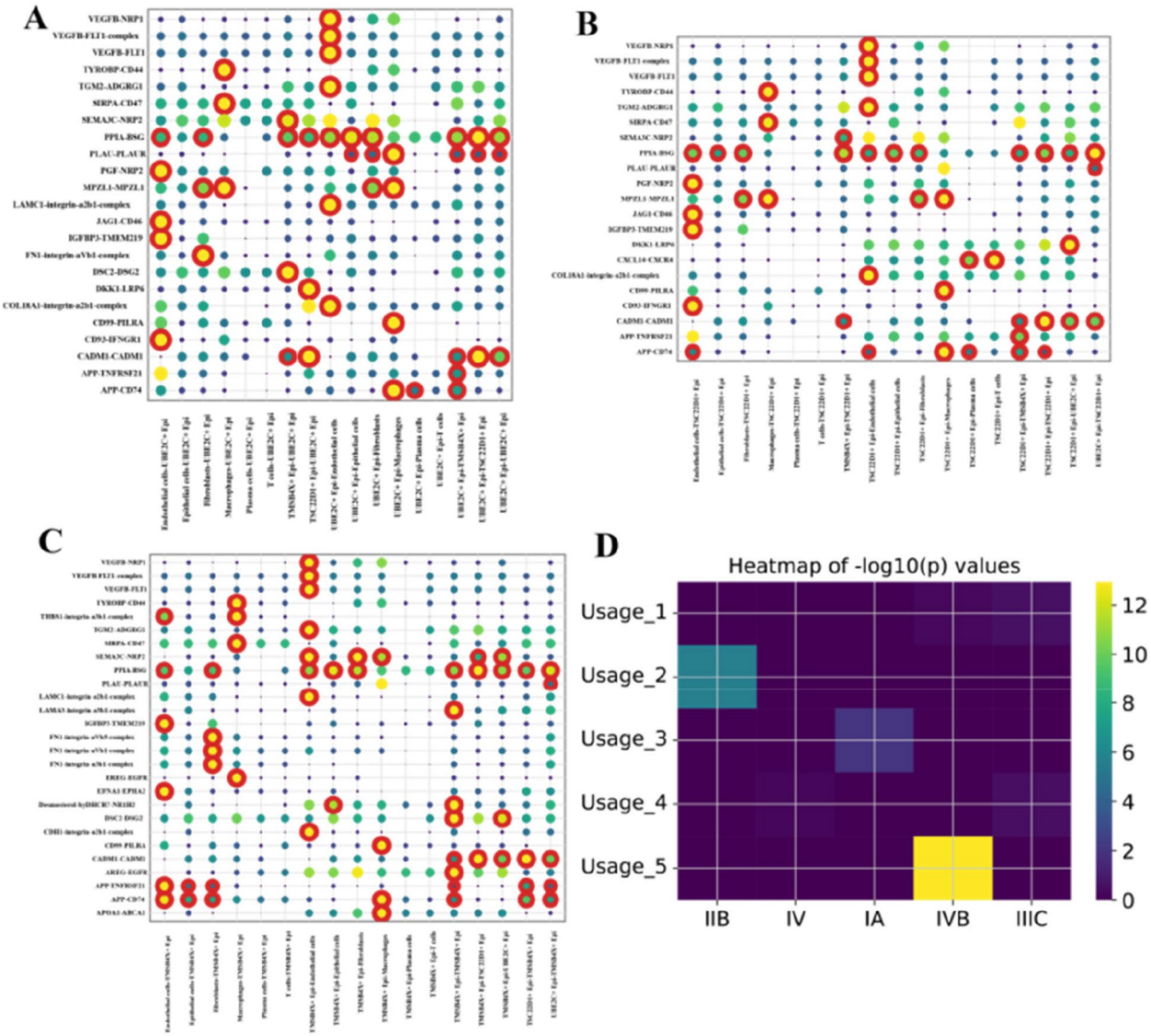

Fig. 5 Subgroup interaction analysis and cNMF-based module identification. **A**–**C** Bubble plots illustrate the intercellular interactions among distinct cell subpopulations, with bubble size and color indicating the significance and strength of each ligand–receptor pair. **D** The heatmap shows the correlation between cNMF (consensus nonnegative matrix factorization) modules and various tumor stages, where brighter colors denote higher significance

and MPZL1-MPZL1) may facilitate immune evasion, while PPIA-BSG and MPZL1-MPZL1 pairs with fibroblasts suggest involvement in ECM regulation. Notably, TSC22D1 + Epi cells engaged in a pronounced CXCL14-CXCR4 interaction with T cells, potentially affecting T-cell chemotaxis and function, thereby exerting a pivotal influence on the immune TME.

Notably, all of 3 epithelial subpopulations shared several frequent interactions with endothelial cells and macrophages, such as VEGFB-NRP1 and TGM2-ADGRG1 (angiogenesis/ECM remodeling), as well as APP-CD74 and CD99-PILRA (immune regulation). Despite their distinct molecular signatures and functional emphases, these subpopulations may converge on core pathways involved in angiogenesis, immune evasion, and stromal reconfiguration, collectively facilitating tumor growth and progression.

Construction and evaluation of the UBE2 C + epi cell related risk signature

We identified that the UBE2C + Epi cells possesses strong stemness and invasive characteristics, potentially

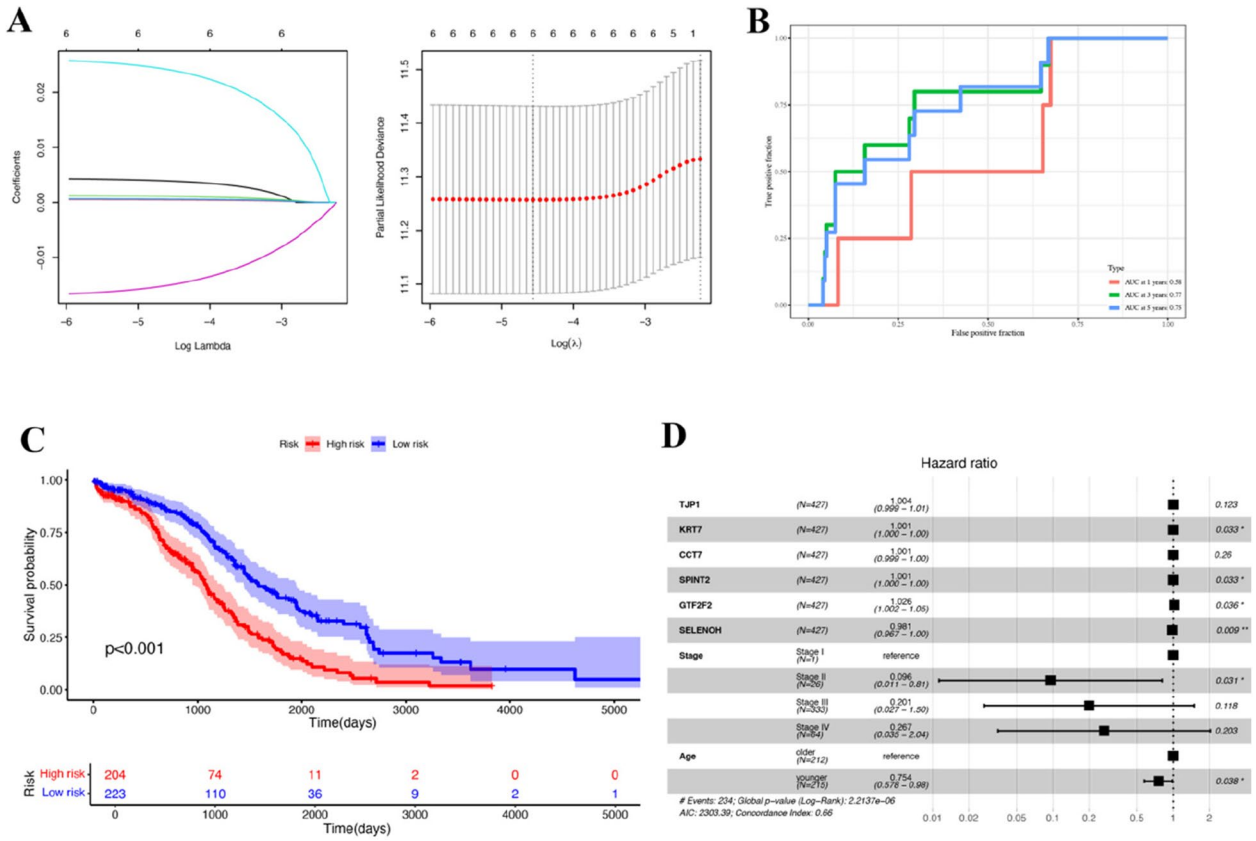

Fig. 6 Construction and evaluation of the UBE2C Risk Score (URS) model. **A** LASSO regression for gene selection. The left panel depicts changes in gene coefficients as the penalty parameter λ (Log Lambda) varies, while the right panel identifies the optimal λ via tenfold cross-validation. **B** Time-dependent ROC curve to evaluate the efficiency of the model. **C** Kaplan–Meier survival analysis between the high and low risk group. **D** Forest plot illustrating the multivariable Cox model results for each gene in the six gene risk signature (TJP1, KRT7, CCT7, SPINT2, GTF2F2, SELENOH), adjusted for age and tumor stage. Hazard ratios (HRs), 95% confidence intervals (CIs), and p-values are shown for each factor, allowing assessment of their independent prognostic significance

representing an early or less-differentiated cell state. To further explore how this subpopulation's gene signature relates to OV outcomes, we constructed a prognostic risk model, aiming to facilitate high risk stratification and guide personalized therapeutic strategies. Using consensus nonnegative matrix factorization (cNMF), we decomposed the gene expression matrix of UBE2C + Epi cells, generating 5 distinct gene modules through consensus clustering (Fig. 5D). Notably, module 5 displayed a significant positive correlation with tumor stage, suggesting its close involvement in disease progression.

To further assess its prognostic potential, we selected the top 200 highly expressed genes within this module for univariate Cox regression analysis. To address multicollinearity and refine the selection of prognostic genes, we performed LASSO regression with ten-fold cross-validation. The cross-validation process involved partitioning the data into ten subsets (folds), training the model on nine of these subsets and validating it on the remaining fold, which was repeated for each fold. This approach helps to mitigate overfitting and improve model generalization. The optimal regularization parameter ($\lambda = 0.002$) was determined based on the lowest cross-validation error (Fig. 6A).

Consequently, six genes, TJP1, KRT7, CCT7, SPINT2, GTF2F2, and SELENOH, emerged as significantly associated with overall survival (OS) ($P < 0.05$). The model's predictive accuracy for 1-, 3-, and 5-year survival was evaluated via ROC curves, yielding AUCs of 0.58, 0.77, and 0.75, respectively (Fig. 6B). While these results indicate moderate discriminatory power over the short and mid-term, the model's overall performance remains suboptimal and warrants further validation in larger, multicenter cohorts.

Subsequently, we incorporated clinical confounders (age and stage) into a multivariable Cox regression to evaluate whether these genes retained prognostic significance (Fig. 6D). Under this adjusted analysis, KRT7,

SPINT2, GTF2F2, and SELENOH remained significantly associated with OS, whereas TJP1 and CCT7 were no longer significant. Notably, GTF2F2 still exhibited a statistically significant association with patient survival (HR = 1.026, 95% CI 1.002–1.05, $p = 0.036$), underscoring its meaningful contribution to prognostic risk. In addition, younger patients showed improved survival outcomes (HR = 0.754, 95% CI 0.578–0.98, $p = 0.038$), and Stage II disease was also associated with better OS relative to Stage I ($p = 0.031$). These findings highlight the importance of adjusting for clinical factors to more accurately delineate each gene's independent prognostic value.

Immune infiltration analysis in different risk group

To further explore differences in the TME between the high and low URS groups, we employed the CIBERSORT method to estimate the relative abundance of various immune cell types (Fig. 7A). The results revealed a distinct distribution of immune cells, with significantly higher proportions of M1 macrophages and follicular helper T cells in the low URS group, whereas resting memory CD4 + T cells were more prevalent in the high URS group. These findings suggest a potential divergence in antitumor immune responses and proliferative regulation between the two risk stratifications. To gain deeper insight into the immune evasion mechanisms, we next compared TIDE scores between groups. To evaluate the degree of immune evasion in each group, we calculated the Tumor Immune Dysfunction and Exclusion scores, focusing on the Exclusion and TIDE indices (Fig. 7B,C). The high URS group exhibited significantly elevated values in both indices, suggesting a heightened propensity for immune evasion and potentially poorer responses to immune checkpoint inhibitors. Accordingly, we next examined correlations between the model's core genes and pivotal immune checkpoint genes to elucidate possible mechanistic links. Furthermore, we conducted a systematic correlation analysis between the 6 prognostic genes in our model and key immune checkpoint genes, such as CTLA4 and PDCD1 (PD-1) (Fig. 7D). We observed both positive and negative correlations, suggesting that different model genes may play distinct roles in regulating immune evasion. These findings underscore the importance of further functional studies to elucidate the mechanisms at play and indicate potential opportunities for targeted interventions in combination with immunotherapy.

The molecular and functional analysis in different risk group

To gain deeper insights into the molecular and functional differences between the high and low URS groups, we performed GSEA, focusing on both GO Biological Process and KEGG pathways (Figs. 8A–B). This approach aims to identify key signaling pathways and molecular functions that may underlie the distinct phenotypes observed in each risk group. At the GO BP level, the high URS group was significantly enriched in the keratinization pathway, suggesting enhanced phenotypic plasticity or differentiation features. By contrast, oxidative phosphorylation was downregulated in the high URS group, implying that low risk tumors may rely more heavily on oxidative metabolism (Fig. 8A). In the KEGG analysis, ECM-receptor interaction was also highly enriched in the high URS group, indicating greater extracellular matrix remodeling and adhesion capacity (Fig. 8B). Meanwhile, the low URS group showed significant upregulation of oxidative phosphorylation and ribosome-related pathways, suggesting a distinct metabolic and protein synthesis preference that may confer alternative survival or adaptation advantages.

We next examined the mutational profiles between the two groups (Figs. 8C–D). In the high URS group, FAT3, USH2A, and AHNAK emerged as the most frequently mutated genes, whereas FLG, MUC16, and NF1 were predominant in the low URS group. Some well known tumor associated genes, including TP53 and CSMD3, exhibited high mutation rates in both groups, though the functional implications warrant further exploration. Additionally, comparison of tumor mutation burden (TMB) revealed significantly higher TMB in the high URS group ($p = 0.00011$, Fig. 8E). Interestingly, survival analysis indicated that patients with elevated TMB had better overall survival ($p = 0.00052$, Fig. 8F), suggesting that while high URS tumors possess a heavier mutational load, they may also benefit from certain therapies, such as immunotherapy, owing to an increased likelihood of generating neoantigens.

We subsequently employed oncoPredict to evaluate the potential responsiveness of the two groups to a range of anticancer agents (Fig. 8G). The high URS group exhibited lower IC50 values for Osimertinib (an EGFR inhibitor), Rapamycin (mTOR pathway inhibitor), and Dihydrorotenone (mitochondrial complex I inhibitor), suggesting increased drug sensitivity. Conversely, ERK inhibitors showed markedly better efficacy in the low URS group, highlighting substantial variations in signaling pathway dependencies and therapeutic responses between the two risk groups. These findings provide preliminary guidance for personalized treatment strategies, though further clinical validation is necessary.

Overall, our analyses reveal pronounced differences between the high and low URS groups at both the genomic and functional levels. The high URS group is characterized by enhanced ECM-receptor interaction,

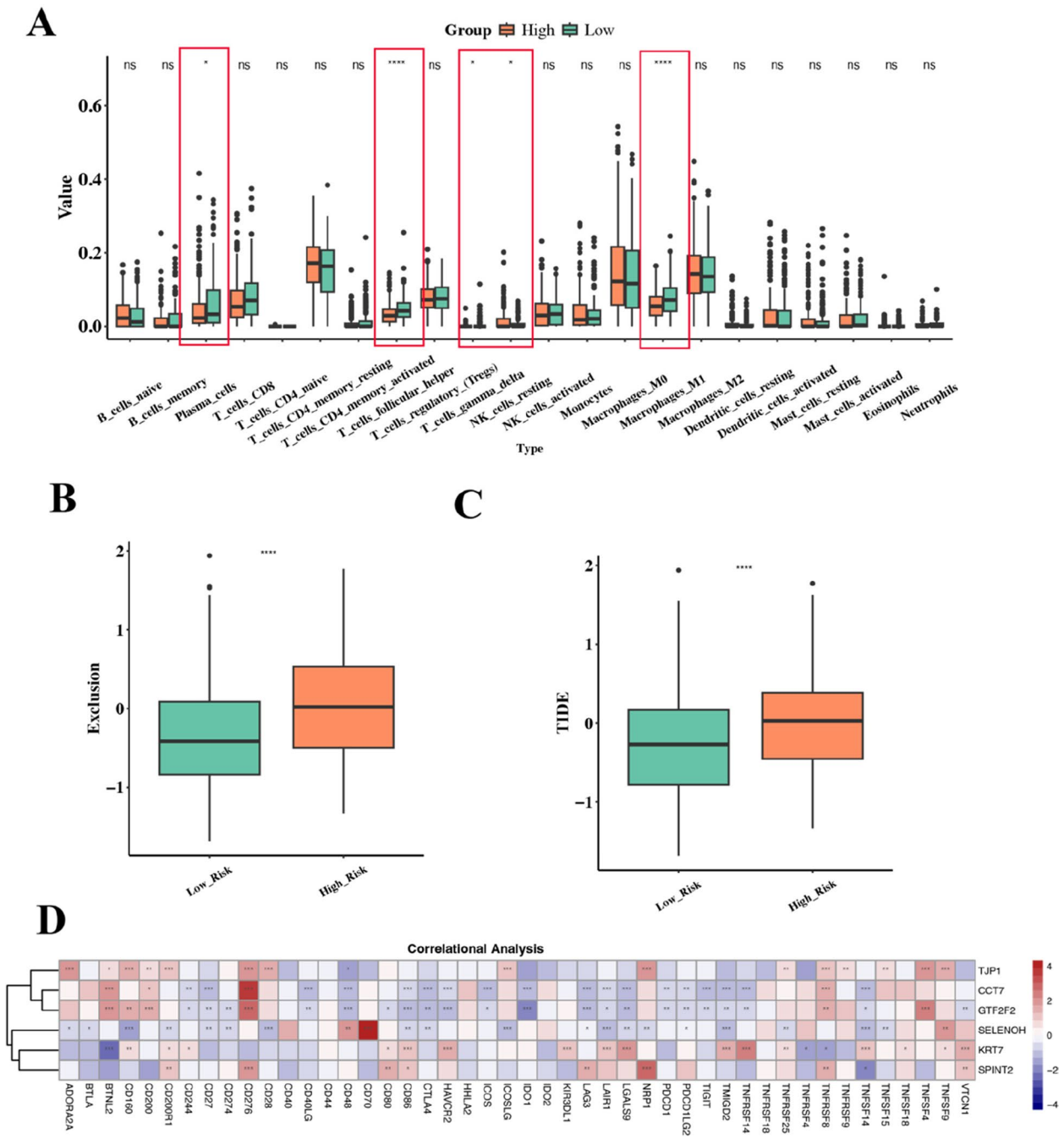

Fig. 7 Analysis of immune infiltration in high and low URS groups. **A** Boxplot illustrating variations in the levels of 22 types of immune infiltrating cells in the high URS group and the low URS group. **B** Boxplot displaying Exclusion values for high and low URS groups. **C** Boxplot displaying TIDE values for high and low URS groups **D** Heatmap displaying the relationship between immune checkpoint genes, prognosis related gene

elevated mutation burden, and specific drug sensitivities, whereas the low URS group exhibits a stronger reliance on oxidative phosphorylation and ribosome biogenesis, along with a more favorable response to ERK inhibition. Such distinct molecular and functional profiles offer valuable insights into the heterogeneity of OV and underscore the potential for stratified treatment approaches. Further clinical and mechanistic investigations are warranted to validate these findings and optimize personalized therapeutic strategies.

Knockdown of GTF2 F2 suppresses the malignant phenotype in OV

To further investigate the functional role of GTF2F2 in OV, we selected the ES-2 cell line and employed short hairpin RNAs (shRNA-1 and shRNA-2) to knock down GTF2F2 expression. Subsequently, we assessed the effects of GTF2F2 knockdown on cell migration and invasion. Wound healing assays demonstrated a marked reduction in wound closure in ES-2 cells following GTF2F2 knockdown, with the shRNA groups exhibiting only 20–40% of the closure rate observed in controls at 48 h ($P < 0.0001$; Fig. 9A). These findings indicate that GTF2F2 is crucial for sustaining the migratory capacity of OV cell. In the Transwell invasion assay, GTF2F2-depleted ES-2 cells exhibited a substantially lower invasion rate, with the number of cells passing through the Matrigel-coated membrane being approximately 50% of that in the control group ($P < 0.001$, Fig. 9B). This finding corroborates the wound healing results, reinforcing the pivotal role of GTF2F2 in facilitating OV cell invasion. Western blot analysis further demonstrated that GTF2F2 knockdown increased E-cadherin levels while reducing N-cadherin, indicating a shift toward a more epithelial phenotype consistent with the observed decrease in cell migratory and invasive abilities (Fig. 10).

Overall, knockdown of GTF2F2 markedly reduced the migratory and invasive capacities of ES-2 cells, in line with our risk model and molecular analyses, thereby underscoring the critical role of GTF2F2 in OV progression.

Discussion

OV currently lacks effective treatment strategies, yet scRNA-seq has presented a crucial opportunity to more precisely interrogate tumor cells and their microenvironment. In this study, we provided a comprehensive characterization of the complex TME in OV by systematically examining the distribution of various cell types across different histological subtypes and clinical stages. We identified 6 major cell types and observed that their proportional distributions varied among subtypes such as Carcinoma, Endometrioid, GST, and High grade serous. Notably, the Endometrioid subtype exhibited a marked low in Macrophage proportional, which does not fully align with previous reports on immune infiltration [19], suggesting the possibility of a unique immune TME. In addition, we found that both T cells and Macrophages undergo significant dynamic changes in advanced disease stages, indicating an active remodeling of the TME during OV progression [20]. These findings offer new perspectives for refining immunotherapeutic approaches and personalizing treatment strategies.

By further focusing on malignant epithelial cells, we identified 4,203 tumor cells through CNV analysis. Based on their gene expression profiles, these cells were grouped into 3 major subpopulations, TMSB4X + Epi, TSC22D1 + Epi, and UBE2C + Epi. GSEA revealed distinct biological features across these subpopulations, TMSB4X + Epi was characterized by enhanced immune evasion and ROS pathways, whereas TSC22D1 + Epi was involved in phospholipid metabolism and estrogen response. In contrast, the UBE2C + Epi subpopulation showed prominent activation of cell cycle related genes (Mitotic Spindle, E2F Targets), along with upregulated EMT and suppressed ROS pathways, indicating stronger adaptability and invasive potential [21]. Notably, the Allograft Rejection pathway was significantly upregulated in the TMSB4X + Epi cell subpopulation. Previous studies in lung cancer and triple-negative breast cancer have shown that activation of this pathway is closely linked to T cell responses triggered by tumor neoantigens, suggesting that these malignant cells can be recognized and attacked by the immune system [22, 23]. Nevertheless, TMSB4X + Epi cells still exhibit tumorigenic properties, implying they may possess certain immune-escape mechanisms or heightened resistance to immunotherapy. This underscores the high degree of heterogeneity within the tumor and opens new avenues for exploring immunotherapeutic interventions. Furthermore, CytoTRACE analysis demonstrated that UBE2C + Epi had the highest stemness score, suggesting a pivotal role in early tumor evolution. UBE2C is closely tied to cell cycle regulation in various solid tumors and serves as a prognostic marker in multiple cancers [24–27]. Consistent with these

(See figure on next page.)

Fig. 8 Analysis of functional differences between the high and low URS groups. **A** GSEA based enrichment analysis of GOBP terms, highlighting significantly enriched pathways. **B** GSEA based enrichment analysis of KEGG pathways, illustrating distinct functional differences between the two groups. **C**–**D** Waterfall plots illustrating mutation profiles in the high and low URS groups, respectively. The bar chart at the top represents the total number of mutations identified in each sample, while the bar on the right side indicates the overall mutation frequency of each gene across samples. **D** Heatmap displaying the relationship between immune checkpoint genes, prognosis related gene. **E** Boxplot displaying TMB values for high and low URS groups. **F** KM survival curves for the high TMB group and the low TMB group. **G** Boxplot showing the difference in drug sensitivity between high and low URS groups

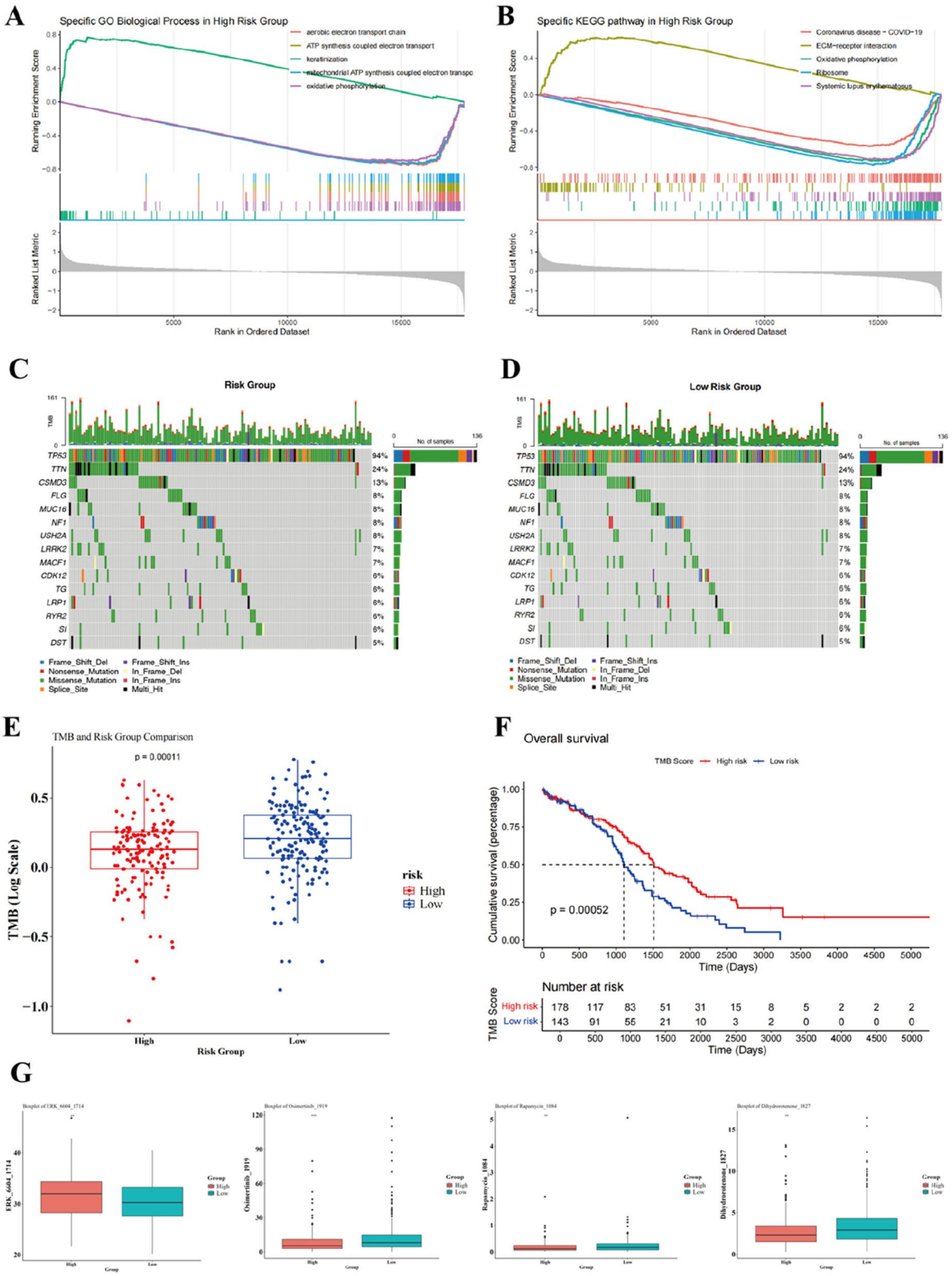

Fig. 8 (See legend on previous page.)

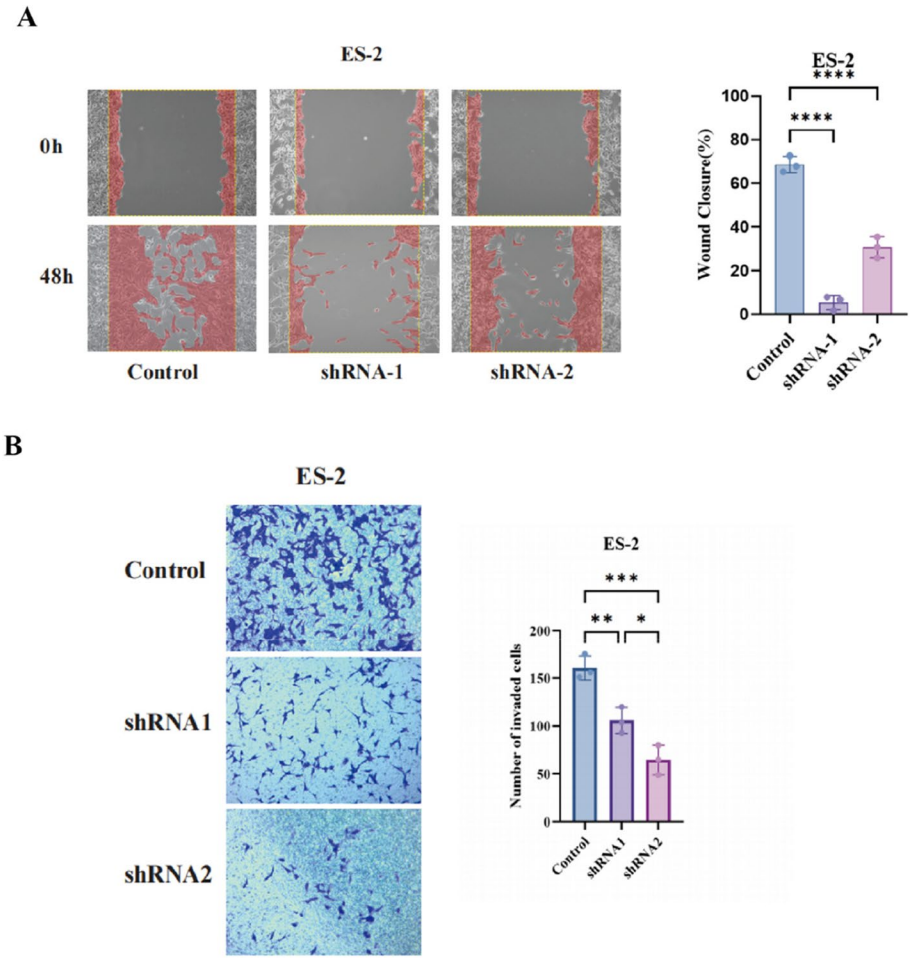

Fig. 9 In vitro experimental validation. **A** The wound healing assay revealed a significant decrease in the migration rate of ES-2 cells with GTF2F2 knockdown. **B** Transwell assay displaying a significant reduction in cell

findings, our results revealed a significant increase in UBE2C + cells during advanced stages, implying heightened invasive capacity.

By integrating pySCENIC data, we found that transcription factors such as MSC (Musculin), NFATC2, and ZBTB24 exhibited higher activity in UBE2C + Epi, potentially driving its stemness and proliferative advantages. Notably, existing research on Musculin has largely centered on its roles in muscle development and T-cell differentiation, and its function within tumor cells has yet to be explored [28, 29]. CellPhoneDB-based cell–cell communication analyses showed abundant ligand–receptor interactions between all three malignant subpopulations and endothelial cells as well as macrophages, including VEGFB–FLT1, TGM2–ADGRG1, APP–CD74, and CD99–PILRA.

Notably, the VEGFB–FLT1 interaction was consistently detected across the subpopulations. VEGFB binding to FLT1 can remodel tumor vasculature by increasing vascular permeability and recruiting pro-tumorigenic macrophages, thereby promoting neovascularization and facilitating immune evasion [30, 31]. Importantly, this pathway operates in a manner partly independent of the classical VEGF-A axis, highlighting its potential as an alternative or complementary target for anti-angiogenic therapy in ovarian cancer, particularly when resistance to VEGF-A blockade occurs. Moreover, the APP–CD74 interaction has been implicated in modulating immune responses. Recent studies indicate that tumor-expressed APP can bind to CD74 on antigen-presenting cells, impairing phagocytic function and enhancing an immunosuppressive microenvironment [32]. Together, these interactions promote angiogenesis, extracellular matrix (ECM) remodeling, and immune evasion [33–36], suggesting a synergistic network shaped by multiple cell types to advance OV progression.

Following an extended cNMF analysis of the UBE2C + epithelial subpopulation, we identified five

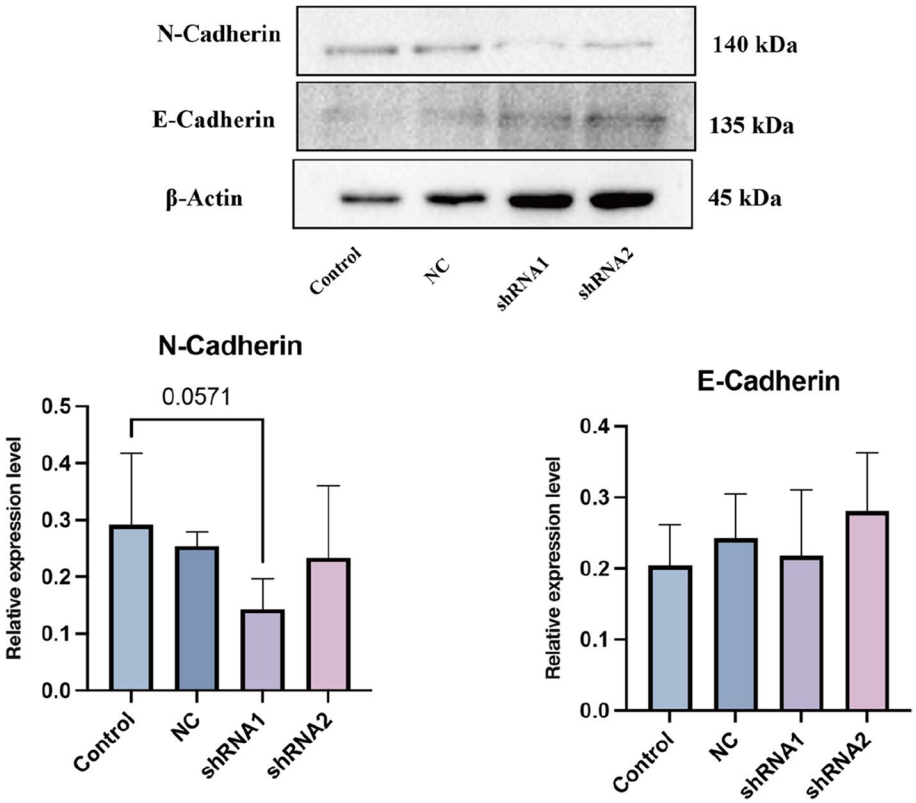

Fig. 10 Western blot and corresponding densitometric analysis of EMT markers following GTF2F2 knockdown. ES-2 cells were transduced with shGTF2F2 or scramble shRNA (shCtrl). The upper panels show the representative Western blot images for E-cadherin and N-cadherin, with β-actin as the loading control. The lower bar chart provides normalized band intensities

distinct gene modules, among which Module 5 showed a positive correlation with OV stage, thus providing a potential molecular stratification reference. Based on Module 5, we employed LASSO regression to establish a six-gene (TJP1, KRT7, CCT7, SPINT2, GTF2F2, and SELENOH) prognostic risk score. While the 3- and 5-year AUC values exceeded 0.70—indicating moderate-to-good predictive power over longer intervals—the 1-year AUC was only 0.58. Notably, gene expression–based prognostic signatures often yield only modest performance in this range, underscoring the intrinsic challenge of predicting complex clinical outcomes using transcriptomic data alone. The relatively low 1-year AUC likely stems from the model's reliance on a single molecular platform (transcriptomics) without incorporating additional molecular or clinical predictors, combined with the inherent heterogeneity of the patient cohort. Future work integrating multi-omics and clinical data may further enhance the model's accuracy and short-term prognostic utility. When stratified into high and low URS groups, marked immunological differences emerged, the high-risk group exhibited a stronger immunosuppressive phenotype, with CD4 + T cells tending toward quiescence and higher TIDE scores, whereas the low-risk group displayed increased M1 macrophage and helper T cell infiltration, indicative of a more active antitumor immune TME. This pattern aligns with previously documented "hot" tumor characteristics [37, 38].

Functional and mutational analyses showed that the high URS group had elevated ECM–receptor interaction pathways and a higher TMB, implying potentially abundant neoantigen formation. However, high TMB does not necessarily confer sensitivity to immunotherapy; indeed, the high-URS group also showed more robust immune evasion, underscoring the need for further assessment of precision treatment feasibility. By contrast, the low URS group relied more on oxidative phosphorylation and exhibited higher sensitivity to ERK inhibitors, suggesting that targeting metabolic vulnerabilities could be a viable treatment approach. With respect to drug sensitivity predictions, the high URS group appeared more responsive to agents such as osimertinib and rapamycin, indicating that different molecular subtypes may benefit from distinct therapeutic strategies. This approach of tailoring drug regimens according to risk scores and

molecular features aligns with current trends in personalized medicine.

Our findings demonstrate that knocking down GTF2F2 in ES2 cells significantly inhibits cell migration, invasion, and the expression of EMT-related proteins, suggesting that GTF2F2 plays a critical role in regulating these processes. Previous studies have shown that, as a key component of the TFIIF complex [39], GTF2F2 not only participates in RNA polymerase II–mediated transcription initiation but also indirectly regulates the cell cycle by ensuring the proper transcription of E2F target genes (such as cyclins and CDKs). Moreover, multiple tumor studies indicate that high GTF2F2 expression is strongly associated with increased cancer stemness and invasiveness, often correlating with poorer clinical outcomes [40]. Taken together, these findings suggest that GTF2F2 may directly or indirectly modulate the cell cycle and E2F signaling, thereby contributing to tumor cell stemness and invasiveness. This provides critical support for our investigation of the UBE2C + epithelial subpopulation, which exhibits heightened stemness and invasive potential.

This study has several limitations. First, our analysis relies mainly on the TCGA OV cohort and one single-cell dataset (GSE173682), lacking validation in larger, independent cohorts. Second, we only performed in vitro assays to assess the function of GTF2F2, and in vivo experiments are needed to confirm its tumor-promoting role. Lastly, while high-grade serous OV (HGSOC) represents themajority of our samples, the applicability of the model across other OV subtypes remains uncertain and warrants further study.

Conclusion

In summary, our research not only unveils the complex heterogeneity of the ovarian cancer TME but also provides a reference framework for subsequent molecular subtyping and refined treatment strategies. Meanwhile, the URS risk model and the functional validation of the key gene GTF2F2 highlight its potential diagnostic and therapeutic value in clinical settings, warranting further in-depth investigation. We believe that an integrated approach combining multi-omics analyses with functional assays will accelerate progress in precision medicine for ovarian cancer, offering renewed hope for improving patient outcomes.

Supplementary Information

The online version contains supplementary material available at https://doi.org/10.1186/s13048-025-01686-3.

Supplementary Material 1.

Supplementary Material 2.

Acknowledgements
Not applicable.

Authors' contributions
Conceptualization, Fuchun Si and Haiyang Du; methodology, Fuchun Si; validation, Haiyang Du and Jiqing Si; formal analysis, Haiyang Du and Gao Si; investigation, Haiyang Du and Jiqing Si; resources, Haiyang Du and Gao Si; data curation, Xuejie Song and Haiyang Du.; writing—original draft preparation, Fuchun Si and Haiyang Du; writing—review and editing, Xuejie Song, Fuchun Si and Haiyang Du; visualization, Gao Si and Jiqing Si; supervision, Fuchun Si and Xuejie Song; project administration, Fuchun Si.; funding acquisition, Fuchun Si. All authors have read and agreed to the published version of the manuscript.

Funding
The research was funded by the Henan science and technology research project (NO.222102310187), Key scientific research projects of universities of Henan Provincial Department of Education (No:21 A360018), 2022 Provincial Science and Technology R&D PlanJoint Fund (cultivation of superior disciplines) (No: 222301420024).

Data availability
No datasets were generated or analysed during the current study.

Code availability
The source code generated or analyzed during the current study is publicly available at Zenodo repository: Https://doi.org/10.5281/zenodo.15105656.

Declarations

Ethics approval and consent to participate
Not applicable.

Consent for publication
Not applicable.

Competing interests
The authors declare no competing interests.

Author details
[1]Traditional Chinese Medicine (Zhong Jing) School, Henan University of Chinese Medicine, Zhengzhou 450046, China. [2]Henan Key Laboratory of TCM Syndrome and Prescription Signaling, Henan International Joint Laboratory of TCM Syndrome and Prescription Signaling, Academy of Chinese Medical Sciences, Henan University of Chinese Medicine, Zhengzhou 450046, China. [3]Department of Orthopedic, The Third Hospital of Peking University, Beijing 100029, China. [4]Henan Hospital of TCM, The Second Affiliated Hospital of Henan University of Traditional Chinese Medicine, Zhengzhou 450046, China.

Received: 18 February 2025 Accepted: 5 May 2025
Published online: 29 May 2025

References

1. Torre LA, Trabert B, DeSantis CE, Miller KD, Samimi G, Runowicz CD, Gaudet MM, Jemal A, Siegel RL. Ovarian Cancer Statistics, 2018. Ca-a Cancer Journal for Clinicians. 2018;68(4):284–96.
2. Kossaï M, Leary A, Scoazec JY, Genestie C. Ovarian Cancer: A Heterogeneous Disease. Pathobiology. 2018;85(1–2):41–9.
3. Odunsi K. Immunotherapy in ovarian cancer. Ann Oncol. 2017;28:1–7.
4. Morand S, Devanaboyina M, Staats H, Stanbery L, Nemunaitis J. Ovarian Cancer Immunotherapy and Personalized Medicine. Int J Mol Sci. 2021;22(12):6532.
5. Wang L, Wang X, Zhu XP, Zhong L, Jiang QX, Wang Y, Tang Q, Li QL, Zhang C, Wang HX, et al. Drug resistance in ovarian cancer: from mechanism to clinical trial. Mol Cancer. 2024;23(1):66.
6. Li JN, Smalley I, Chen ZH, Wu JY, Phadke MS, Teer JK, Nguyen T, Karreth FA, Koomen JM, Sarnaik AA, et al. Single-cell Characterization of the Cellular

Landscape of Acral Melanoma Identifies Novel Targets for Immunotherapy. Clin Cancer Res. 2022;28(10):2131–46.
7. Yeo AT, Rawal S, Delcuze B, Christofides A, Atayde A, Strauss L, Balaj L, Rogers VA, Uhlmann EJ, Varma H, et al. Single-cell RNA sequencing reveals evolution of immune landscape during glioblastoma progression. Nat Immunol. 2022;23(6):971.
8. Moorman AR, Benitez EK, Cambuli F, Jiang Q, Mahmoud A, Lumish M, Hartner S, Balkaran S, Bermeo J, Asawa S, et al. Progressive plasticity during colorectal cancer metastasis. Nature. 2025;637(8047):947–54.
9. González-Silva L, Quevedo L, Varela I. Tumor Functional Heterogeneity Unraveled by scRNA-seq Technologies. Trends in Cancer. 2020;6(1):13–9.
10. Wolf FA, Angerer P, Theis FJ. SCANPY: large-scale single-cell gene expression data analysis. Genome Biol. 2018;19:1–5.
11. Korsunsky I, Millard N, Fan J, Slowikowski K, Zhang F, Wei K, Baglaenko Y, Brenner M, Loh PR, Raychaudhuri S. Fast, sensitive and accurate integration of single-cell data with Harmony. Nat Methods. 2019;16(12):1289.
12. Kang M, Armenteros JJA, Gulati GS, Gleyzer R, Avagyan S, Brown EL, Zhang W, Usmani A, Earland N, Wu Z, Zou J, Fields RC, Chen DY, Chaudhuri AA, Newman AM. Newman: Mapping single-cell developmental potential in health and disease with interpretable deep learning. BioRxiv, 2024: 2024.03. 19.585637.
13. Aibar S, González-Blas CB, Moerman T, Van AHT, Imrichova H, Hulselmans G, Rambow F, Marine JC, Geurts P, Aerts J, et al. SCENIC: single-cell regulatory network inference and clustering. Nat Methods. 2017;14(11):1083.
14. Efremova M, Vento-Tormo M, Teichmann SA, Vento-Tormo R. Cell PhoneDB: inferring cell-cell communication from combined expression of multi-subunit ligand-receptor complexes. Nat Protoc. 2020;15(4):1484–506.
15. Newman AM, Liu CL, Green MR, Gentles AJ, Feng WG, Xu Y, Hoang CD, Diehn M, Alizadeh AA. Robust enumeration of cell subsets from tissue expression profiles. Nat Methods. 2015;12(5):453.
16. Wu TZ, Hu EQ, Xu SB, Chen MJ, Guo PF, Dai ZH, Feng TZ, Zhou L, Tang WL, Zhan L et. al: clusterProfiler 4.0: A universal enrichment tool for interpreting omics data. Innovation 2021;2(3).
17. Mayakonda A, Lin DC, Assenov Y, Plass C, Koeffler HP. Maftools: efficient and comprehensive analysis of somatic variants in cancer. Genome Res. 2018;28(11):1747–56.
18. Geeleher P, Cox N, Huang RS. pRRophetic: An R Package for Prediction of Clinical Chemotherapeutic Response from Tumor Gene Expression Levels. Plos One. 2014;9(9):e107468.
19. Artemova D, Vishnyakova P, Elchaninov A, Gantsova E, Sukhikh G, Fatkhudinov T. M1 macrophages as promising agents for cell therapy of endometriosis. Heliyon. 2024;10(16).
20. Drakes ML, Stiff PJ. Regulation of Ovarian Cancer Prognosis by Immune Cells in the Tumor
21. Liu J, Peng YH, Wei WY. Cell cycle on the crossroad of tumorigenesis and cancer therapy. Trends Cell Biol. 2022;32(1):30–44.
22. Oshi M, Patel A, Wu R, Le L, Tokumaru Y, Yamada A, Yan L, Matsuyama R, Ishikawa T, Endo I, et al. Enhanced immune response outperform aggressive cancer biology and is associated with better survival in triple-negative breast cancer. Npj Breast Cancer. 2022;8(1):92.
23. Zhang J, Song C, Tian Y, Yang X. Single-Cell RNA Sequencing in Lung Cancer: Revealing Phenotype Shaping of Stromal Cells in the Microenvironment. Front Immunol. 2022;12:802080.
24. Nicolau-Neto P, Palumbo A, De Martino M, Esposito F, Simio TD, Fusco A, Nasciutti LE, Da Costa NM, Pinto LFR. *UBE2C* Is a Transcriptional Target of the Cell Cycle Regulator FOXM1. Genes. 2018;9(4):188.
25. Lu ZN, Song J, Sun TH, Sun G. UBE2C affects breast cancer proliferation through the AKT/mTOR signaling pathway. Chin Med J. 2021;134(20):2465–74.
26. Liu GL, Zhao J, Pan BY, Ma G, Liu LR. UBE2C overexpression in melanoma and its essential role in G2/M transition. J Cancer. 2019;10(10):2176–84.
27. Chen ZP, Wang LF. The clinical significance of *UBE2C* gene in progression of renal cell carcinoma. Eur J Histochem. 2021;65(2):3196.
28. Yu J, Liu YJ, Zhang W, Yang X, Tang WQ, Liang HP, Li SY, Gao WD, Yan J. Musculin Deficiency Aggravates Colonic Injury and Inflammation in Mice with Inflammatory Bowel Disease. Inflammation. 2020;43(4):1455–63.
29. Wu C, Chen ZJ, Dardalhon V, Xiao S, Thalhamer T, Liao MY, Madi A, Franca RF, Han T, Oukka M, et al. The transcription factor musculin promotes the unidirectional development of peripheral T_{reg} cells by suppressing the T_H2 transcriptional program. Nat Immunol. 2017;18(3):344–53.
30. Yang X, Zhang Y, Hosaka K, Andersson P, Wang J, Tholander F, Cao Z, Morikawa H, Tegner J, Yang Y, et al. VEGF-B promotes cancer metastasis through a VEGF-A-independent mechanism and serves as a marker of poor prognosis for cancer patients. Proc Natl Acad Sci USA. 2015;112(22):E2900–9.
31. Lee C, Chen R, Sun G, et al. VEGF-B prevents excessive angiogenesis by inhibiting FGF2/FGFR1 pathway. Signal Transduct Target Ther. 2023;8(9):4380–93.
32. Chen G, Wang W, Wei X, Chen Y, Peng L, Qu R, Luo Y, He S, Liu Y, Du J, et al. Single-cell transcriptomic analysis reveals that the APP-CD74 axis promotes immunosuppression and progression of testicular tumors. Journal of Pathology. 2024;264(3):250–69.
33. Teleanu RI, Chircov C, Grumezescu AM, Teleanu DM. Tumor Angiogenesis and Anti-Angiogenic Strategies for Cancer Treatment. J Clin Med. 2020;9(1):84.
34. Rajabi M, Mousa SA. The Role of Angiogenesis in Cancer Treatment. Biomedicines. 2017;5(2):34.
35. Mohan V, Das A, Sagi I. Emerging roles of ECM remodeling processes in cancer. Semin Cancer Biol. 2020;62:192–200.
36. Vinay DS, Ryan EP, Pawelec G, Talib WH, Stagg J, Elkord E, Lichtor T, Decker WK, Whelan RL, Kumara H, et al. Immune evasion in cancer: Mechanistic basis and therapeutic strategies. Semin Cancer Biol. 2015;35:S185–98.
37. Galon J, Bruni D. Approaches to treat immune hot, altered and cold tumours with combination immunotherapies. Nat Rev Drug Discovery. 2019;18(3):197–218.
38. Yang YQ, Zhao TJ, Chen QH, Li YM, Xiao ZX, Xiang YT, Wang BY, Qiu YG, Tu SQ, Jiang YT, et al. Nanomedicine Strategies for Heating "Cold" Ovarian Cancer (OC): Next Evolution in Immunotherapy of OC. Adv Sci (Weinh). 2022;9(28):2202797.
39. Cao C, Luo Z, Zhang H, Yao S, Lu H, Zheng K, Wang Y, Zou M, Qin W, Xiong H, et al. A methylation-related signature for predicting prognosis and sensitivity to first-line therapies in gastric cancer. Journal of Gastrointestinal Oncology. 2023;14(6):2354–72.
40. Minchenko OH, Tsymbal DO, Minchenko DO, Kubaychuk OO. Hypoxic regulation of MYBL1, MEST, TCF3, TCF8, GTF2B, GTF2F2 and SNAI2 genes expression in U87 glioma cells upon IRE1 inhibition. Ukrainian biochemical journal. 2016;88(6):52–62.

Publisher's Note